Search for a structural response to the intermediate phase in Ge_xSe_{1-x} glasses

Moneeb T. M. Shatnawi,[1,*] Christopher L. Farrow,[1] Ping Chen,[2] Punit Boolchand,[2] Asel Sartbaeva,[3] M. F. Thorpe,[3] and Simon J. L. Billinge[1,†]

[1]*Department of Physics and Astronomy, Michigan State University, East Lansing, Michigan 48824, USA*

[2]*Department of ECECS, The University of Cincinnati, Ohio 45221, USA*

[3]*Department of Physics, Arizona State University, Tempe, Arizona 85287, USA*

(Received 17 September 2007; published 26 March 2008)

Atomic pair distribution functions (PDFs) obtained from high energy x-ray synchrotron radiation and x-ray absorption fine structure measurements were performed on 18 closely spaced compositions of chalcogenide glasses (Ge_xSe_{1-x} with $0.15 \leq x \leq 0.40$), which span the range of the floppy to rigid phase transition in these glasses. Structural parameters such as PDF peak widths, Debye–Waller factors from extended x-ray absorption fine structure, and the first sharp diffraction peak in $S(Q)$ were extracted as a function of composition. These parameters smoothly evolve with composition, but there are no clear discontinuities or breaks in the slope associated with the appearance of the intermediate phase (IP). Therefore, these measurements do not confirm a structural origin for the IP.

DOI: 10.1103/PhysRevB.77.094134 PACS number(s): 61.43.Fs, 61.43.Dq, 61.05.cp, 81.05.Kf

I. INTRODUCTION

According to constraint counting theory,[1,2] a network is considered floppy if the average number of constraints per atom (n_c) is less than 3 (the number of degrees of freedom for an atom in three dimensions), as in the case of twofold coordinated single bond chain networks. On the other hand, the network is rigid if n_c is greater than 3, as in networks consisting only of tetrahedral units (such as SiO_2). Thus, a progressive addition of cross-linking elements (such as Si, As, or Ge) to a starting chain network (such as S or Se) will result in a progressive increase in its connectivity [mean coordination number ($\bar{r}$)]. At $\bar{r}=2.4$, rigidity percolation occurs, where the network changes from a floppy to a rigid structure.[3] A number of experiments[4–6] show responses consistent with a percolation transition.

Canonical systems for studying this phenomenon are the chalcogenide glasses. Surprisingly, based on thermodynamic and spectroscopic measurements, they appear to exhibit two transitions instead of one.[7] The region between these transitions has been called the intermediate phase (IP).[7,8] The original theoretical work assumed that the network was generic and the connectivity was random.[3] Therefore, it was suggested[11] that the IP phase is a region of finite width in composition, where the network could self-organize in such a way that it maintains a rigid but unstressed state. Recent theoretical work suggested that the IP can be usefully thought of as being poised at criticality throughout the IP.[9] The agglomeration model can also be used to gain further insight into the formation mechanisms associated with the IP.[10] Recently, it was also confirmed[12] that a self-organization in the lengths of the Se chains connecting nodal (Ge) atoms can lead to a wide IP window in models of the GeSe system. However, it was proven very difficult to experimentally establish this result. If this interpretation is correct, we expect to see a direct structural response to the transitions. It should be apparent in structural parameters sensitive to strain, since it is a transition from an unstressed to a stressed state. Self-organization in the IP may also be apparent by observing the appearance of an intermediate range structural order, for example, changes in the first sharp diffraction peak (FSDP).

To test the hypothesis of the IP, we have made a study of a series of carefully prepared glasses in the Ge_xSe_{1-x} system. This system can be made as glasses over a wide composition range ($x=0.0-0.42$ at. % germanium),[13–16] allowing the systematic composition dependence to be studied. In this paper, we present a detailed systematic composition dependent study of structural parameters in Ge_xSe_{1-x} alloys covering a wide range of composition around the IP ($0.15 \leq x \leq 0.40$) with a narrow spacing between points. X-ray diffraction data were measured using advanced high energy synchrotron radiation with complementary x-ray absorption fine structure (XAFS) measurements.

The diffraction data have been processed to obtain the total scattering structure function $S(Q)$ and the reduced pair distribution function (PDF). The width of the first peak in the PDF, which contains information about strain in the system, has been extracted as a function of composition x. We have also extracted information about intermediate range order (IRO) from the FSDP vs x. A study by Sharma *et al.*[17] indicated that the position and width of the FSDP in this system have an anomaly in the region of the IP, from which they proposed the existence of three well resolved structural regions consistent with the IP. This result was not reproduced in our work. In fact, we do not see any clear structural responses from the PDF and XAFS data that correlate with the expected appearance of the IP.

II. EXPERIMENTAL PROCEDURES AND DATA REDUCTION

Bulk glass samples of Ge_xSe_{1-x}, where $x=0.15$, 0.16, 0.18, 0.19, 0.20, 0.21, 0.22, 0.23, 0.24, 0.26, 0.28, 0.30, 0.33, 0.34, 0.35, 0.36, 0.38, and 0.40, were prepared by a conventional melt quenching process. The starting ingredients (99.9999% Ge and Se) were vacuum sealed (5×10^{-7} Torr) in quartz tubes and heated to 950 °C for 4 days or more.

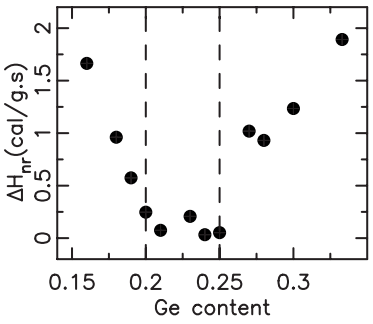

FIG. 1. The nonreversing heat flow (ΔH_{nr}) vs composition for the samples used in this study. The results indicate that these samples exhibit the experimental signature associated with the presence of an IP (Ref. 7), which can be located from this plot in the region $0.2<x<0.25$.

Melt temperatures were then slowly lowered to 50 °C above the liquidus, where they equilibrated for 6 h before quenching in cold water. Samples were allowed to age for 3 weeks before the quartz tubes were opened, and glass transitions were examined in modulated differential scanning calorimetric (m-DSC) measurements. A scan rate of 3 °C/min and a modulation rate of 1 °C/100 s were used to record scans. The frequency corrected nonreversing enthalpy $\delta H_{nr}(x)$ for the samples was measured and showed a square-well-like global minimum, as shown in Fig. 1. As in earlier studies,[18] there is a clear minimum in H_{nr}, which is used as an indicator for the IP and the quality of the samples. Great care was taken to ensure sample homogeneity. m-DSC can determine if a sample is homogeneously alloyed by looking at different parts of a batch preparation and measuring the glass transition temperature (T_g).[19] These samples were alloyed long enough to ensure that they were homogeneous and then tested for homogeneity by looking at several parts of the same batch to see if T_g's were the same.

Preliminary results on a subset of the samples have been reported in Ref. 20. The glasses were gently crushed into fine powder, formed into disks 5 mm in diameter and 1 mm thick, sealed between thin Kapton foils, and subjected to x-ray diffraction experiments. This approach ensured that the samples in the beam were of uniform geometry.

The x-ray diffraction measurements were carried out using the rapid acquisition PDF technique[21] at the MUCAT 6-ID-D beamline at the Advanced Photon Source (APS), Argonne National laboratory, at room temperature. A bent double-Laue Si (111) crystal[22] was used to monochromatize the white beam and deliver an intense flux of x-ray photons of energy 87.005 keV ($\lambda=0.142\,50$ Å). A large area image plate detector (MAR345) was placed 108 mm behind the sample. The sample-detector distance was calibrated using a silicon standard of known lattice parameter. The use of x rays of such high energy allows the access of higher wave vectors and helps reduce several unwanted experimental effects, such as absorption and multiple scattering. Five diffraction scans, with an irradiation time of 100 s each, were conducted for each sample and the diffracted intensities were averaged to improve the statistical accuracy and reduce any systematic effects due to instabilities in the experimental setup. The integration of the MAR images was performed using the program FIT2D.[23] Data reduction to obtain the structure functions, $S(Q)$'s, and the PDF, $G(r)$'s, were performed using the program PDFGETX2.[24]

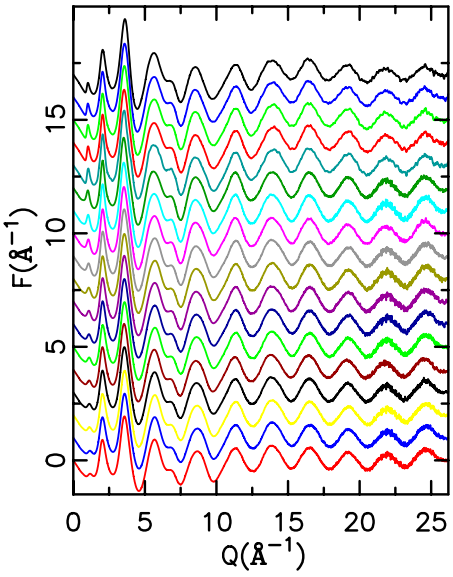

FIG. 2. (Color online) The measured structure functions, $F(Q)=Q[S(Q)-1]$, for the Ge_xSe_{1-x} glasses. Data are offset for clarity. The compositions (x) are, from the bottom to the top curves, 0.15, 0.16, 0.18, 0.19, 0.20, 0.21, 0.22, 0.23, 0.24, 0.26, 0.28, 0.30, 0.33, 0.34, 0.35, 0.36, 0.38, and 0.40.

The structure function $S(Q)$ is related to the coherent part of the total diffracted intensity of the material and is given by

$$S(Q)=\frac{I^{coh}(Q)-\Sigma c_i|f_i(Q)|^2}{|\Sigma c_i f_i(Q)|^2}+1, \tag{1}$$

where $I^{coh}(Q)$ is the measured scattering intensity from a powder sample that has been properly corrected for background and other experimental effects and normalized by the flux and number of atoms in the sample. Here, c_i and f_i are the atomic concentration and x-ray atomic form factor, respectively, for the atomic species of type i.[25,26] Figure 2 shows the measured reduced structure functions, $F(Q)=Q[S(Q)-1]$, for all of the studied Ge_xSe_{1-x} glasses.

The overall similarity of the $F(Q)$ curves indicates that there is no appreciable unaccounted background or systematic effects interfering with the signal from the sample. The overall shapes of the curves (including the oscillations about zero at high Q) are remarkably similar, suggesting that the data reduction and normalization procedures are effective. The curves have not been smoothed and the low level of noise, even at high Q, is apparent.

The data were then Fourier transformed to obtain the reduced pair distribution functions, $G(r)$'s, and these are shown in Fig. 3. From the experimental PDFs shown in Fig. 3, we see a relatively small number of well-defined peaks, which is a signature of such glassy materials since the stronger the disorder in a noncrystalline material, the weaker the correlations between the positions of the atoms in it and,

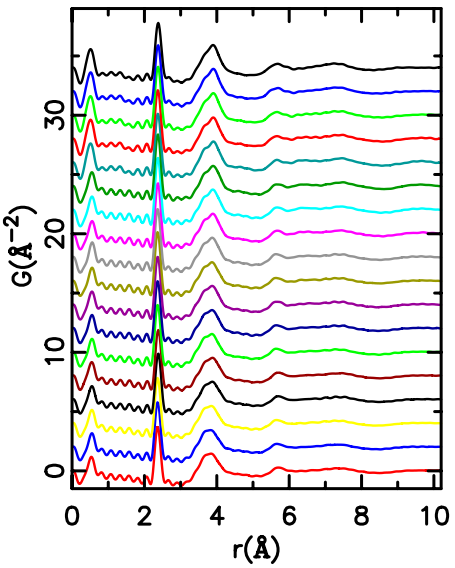

FIG. 3. (Color online) Experimental atomic PDF $G(r)$s for Ge_xSe_{1-x} glasses. Data are offset for clarity. The compositions (x) are, from the bottom to the top curves, 0.15, 0.16, 0.18, 0.19, 0.20, 0.21, 0.22, 0.23, 0.24, 0.26, 0.28, 0.30, 0.33, 0.34, 0.35, 0.36, 0.38, and 0.40.

hence, the lower the number of well-defined peaks in the PDF. The peaks occurring at short distances (below the first PDF peak at 2.37 Å) are unphysical and are due to imperfections in the data reduction.

The Ge_xSe_{1-x} glasses were also subjected to XAFS measurements. Finely powdered glasses were uniformly spread on adhesive Scotch tape. About 8–12 layers were stacked to get optimized signal-to-noise levels. The XAFS measurements were performed in the transmission mode at the bending magnet beamline, 5BM-D, at the Advanced Photon Source, using Si ⟨111⟩ double crystal monochromator. The energy resolution of the monochromatic beam was determined to be ~1.5 eV for a near-edge structure and about 3 eV for the extended x-ray absorption fine structure (EXAFS). A beam size of about 0.3×0.5 mm^2 was used, resulting in an incident photon flux of $\sim10^{10}$ photons per second. The synchrotron storage ring was operated in the top-up mode, with the electron beam current kept of around 100 mA.

The monochromator was scanned in energy from 200 eV below to 800 eV above the Ge and Se K-absorption edges (11 103 and 12 659 eV, respectively). The incident I_0 and the transmitted I_t x-ray intensities were measured simultaneously at room temperature by using ion chambers located before and after the sample. The ion chambers were filled with a mixture of nitrogen and argon gases. Data were collected with a step size of 0.2 eV in the respective edge regions. The energy calibrations were performed by using Ge and Se foils between the I_t and a third, I_{ref}, ion chamber, respectively.

The EXAFS data reduction was performed by using standard procedures using the ATHENA software package.[27,28] The measured absorption spectrum below the preedge region was fitted to a straight line. The AUTOBK algorithm[29] implemented in ATHENA was used to determine the background and normalize the x-ray absorption, $\mu(E)$, data. This algorithm uses a cutoff parameter (Rbkg) to define the Fourier frequency, below which the signal is dominated by the background and above which the signal contains the data. Thus, AUTOBK attempts to remove those Fourier components that are due to the background while leaving those that contain the data.

Edge step normalization was also done by the ATHENA software, where the difference between the raw data, $\mu(E)$, and the background, $\mu_0(E)$, is divided by an estimation of the edge step value $[\mu_0(E_0)]$ resulting in the EXAFS signal, $\chi(E)$, which is defined by the following relation:

$$\chi(E) = \frac{\mu(E) - \mu_0(E)}{\mu_0(E_0)}. \tag{2}$$

The normalized $\chi(E)$ spectra were then converted to $\chi(k)$ in k space, $k=[8\pi^2 m(E-E_0)/h^2]^{1/2}$. The resulting $\chi(k)$ functions were then weighted with k^2 to account for the damping of oscillations with increasing k. Based on this, the formula describing the EXAFS can be calculated and, in a.u., is given by[30]

$$\chi(k) = -\sum_j \frac{N_j}{R_j^2}\frac{|f_j(\pi)|}{k}\exp\left(-\frac{2R_j}{\lambda_e}\right)\exp(-2\sigma_j^2k^2)\sin[2kR_j + 2\delta(k) + \eta_j(k)], \tag{3}$$

where a sum over all shells of atoms j is taken, each containing N_j atoms at a distance R_j from the absorbing atom. $|f_j(\pi)|$ is the backscattered amplitude from the atoms in the jth shell, λ_e is the finite mean free path of the electrons in the material, and σ_j is the Debye–Waller term involving root mean square displacements (static or thermal) about the equilibrium position. The amplitude of the EXAFS is sinusoidally modulated by a function involving the phase shift of the electron; the additional phase shifts $\delta(k)$ and $\eta(k)$ arise because the photoelectron is emitted and backscattered, respectively, from atomic potentials. Figure 4 shows the XAFS $k^2\chi(k)$ for all the studied samples at both Ge and Se edges. The pure oscillations in $k^2\chi(k)$ are consistent with such a glassy material, in which they result in a single well-defined shell after being Fourier transformed.

The radial structure function $\phi(r)$ was then obtained via Fourier transformation given by

$$\phi(r) = \frac{1}{(2\pi)^{1/2}}\int_{k_{min}}^{k_{max}} \chi(k)M(k)k^n \exp(2ikr)dk \tag{4}$$

of the normalized k^2-weighted EXAFS spectra, $k^2\chi(k)$, using a k range of 2.5–15.9 Å^{-1} for both Ge and Se edges. Here, $M(k)$ is a window function, and n represents the k weight used.

The Fourier transforms of the measured EXAFS signals at both Ge and Se edges are shown in Fig. 5. The Fourier transforms at both Ge and Se K edges clearly show a well-defined first shell, as expected, but the second and higher order shells appear to be observable at a level only slightly above the noise level. This decreased information in the higher shells

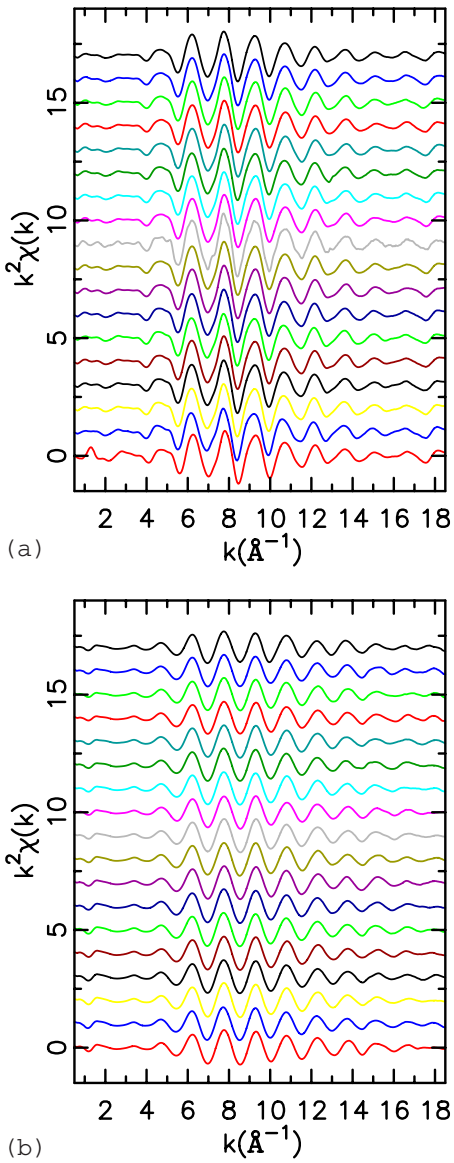

FIG. 4. (Color online) k^2-weighted XAFS signal $[k^2\chi(k)]$ for Ge_xSe_{1-x} glasses at the (a) Ge edge and (b) Se edge. Data are shifted up for clarity. The compositions (x) are, from the bottom to the top curves, 0.15, 0.16, 0.18, 0.19, 0.20, 0.21, 0.22, 0.23, 0.24, 0.26, 0.28, 0.30, 0.33, 0.34, 0.35, 0.36, 0.38, and 0.40.

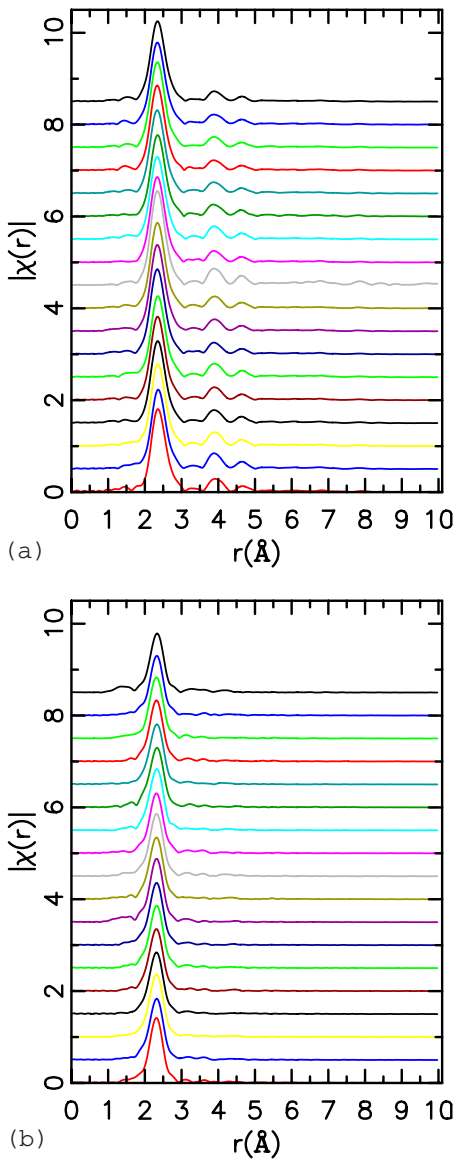

FIG. 5. (Color online) Magnitude of the Fourier transform of k^2-weighted XAFS signals $[k^2\chi(k)]$ for Ge_xSe_{1-x} glasses at the (a) Ge edge and (b) Se edge. Data are shifted up for clarity. The compositions (x) are, from the bottom to the top curves, 0.15, 0.16, 0.18, 0.19, 0.20, 0.21, 0.22, 0.23, 0.24, 0.26, 0.28, 0.30, 0.33, 0.34, 0.35, 0.36, 0.38, and 0.40.

reflects the fact that the considerable disorder (which manifests itself in large Debye–Waller factors) plays a dominant role in these glasses.

EXAFS data fitting was performed using the ARTEMIS program.[28] A single scattering path was used to fit each bond type. For Ge-edge data, Ge-Se and Ge-Ge single scattering paths were used, and for the Se-edge data, Se-Ge and Se-Se single scattering paths were used.

III. RESULTS AND DISCUSSION

The transition from floppy to rigid in Ge_xSe_{1-x} glasses should be accompanied by the appearance of strain in the overconstrained region above the transition. One explanation for the appearance of the intermediate phase is that, due to self-organization of the network, there is a region of finite composition width that is rigid but unstrained.[11] A measurement of the residual strain state of the glass could give a direct support to this picture. In the PDF, a homogeneous strain can be detected as a shift in bond length (PDF peak position) and inhomogeneous strain as a broadening of the bond-length distribution. The first peak in the PDF yields direct information about bond stretching in the nearest neighbor bonds. Changes in peak positions and widths of higher order peaks yield information about bond-bending relaxations in covalent systems.[31,32] Things are complicated in the glass because of a peak overlap between peaks of different structural origins. Nonetheless, it is still interesting to look

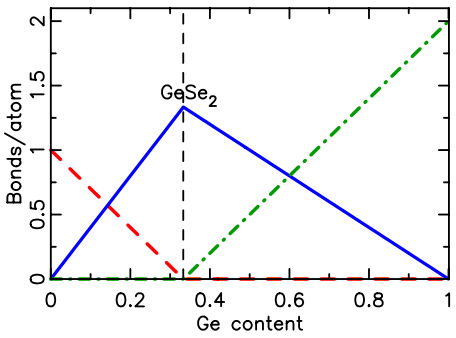

FIG. 6. (Color online) Bond counting statistics for a 4–2 Ge_xSe_{1-x} network based on the CON model. Red (dashed), blue (solid), and green (dot-dashed) curves represent Se-Se, Ge-Se, and Ge-Ge bonds, respectively. The dashed vertical line is plotted at the stoichiometric composition ($GeSe_2$).

for evidence of strain in these glasses. Initially, we just consider the nearest neighbor PDF peak.

The first PDF peak in Ge_xSe_{1-x} glasses is a multicomponent peak. It has three unresolved contributions: $r_{Se\text{-}Se}=2.32$ Å, $r_{Ge\text{-}Se}=2.37$ Å, and $r_{Ge\text{-}Ge}=2.42$ Å. The relative intensities of these are determined by the Ge content of the glass. At the low Ge contents of interest, we expect the peak to be dominated by Se-Se and Ge-Se correlations. The contribution of each of these subpeaks can be estimated by using the chemically ordered network (CON) model proposed for Ge_xSe_{1-x} glasses.[33] This model emphasizes the relative bond energies and is based on an assumption that heteropolar or Ge-Se bonds are favored at all compositions. The CON model contains a chemically ordered compound phase at a composition $x_c=N_{Se}/(N_{Ge}+N_{Se})$, where N_i is the coordination number of an atom of type i. This phase is the $GeSe_2$, or $x=0.33$, in this case. This chemically ordered compound (according to the CON model) contains only Ge-Se bonds. For compositions with larger Se content than the $GeSe_2$ compound, the alloys contain Ge-Se and Se-Se bonds; whereas for compositions with higher Ge content, the alloys contain Ge-Se and Ge-Ge bonds. Figure 6 displays the bond counting statistics for the Ge_xSe_{1-x} alloys based on the CON model. In the region of interest, for compositions in the vicinity of the IP, the CON model predicts only Ge-Se and Se-Se bonds to be present. The width of the bond distributions is expected to be ~0.1 Å at room temperature, whereas the separation of the centroids of the two peaks is expected to be $r_{Ge\text{-}Se}-r_{Se\text{-}Se}=0.05$ Å. The intrinsic width of the peaks is greater than the separation of the peaks and the subcomponents are not resolved. Indeed, the intrinsic width of the subcomponents dominates the observed PDF peak width and results in a peak that is quite Gaussian in its intrinsic shape, convoluted with the Sinc function coming from the finite termination of the data in Q space, as observed in Fig. 3. In analyzing the first PDF peak, we have extracted its parameters from both experimental and simulated data. In particular, we have fitted it with a single Gaussian convoluted with a Sinc function to simulate the finite Q_{max} of the measurement.

The width of the first PDF peak contains the desired information about peak broadening due to strain effects, but because it contains more than one unresolved bond, its position, width, and intensity also evolve due to the changing composition of the network. In order to separate these effects, we simulate the first PDF peak taking into account the changing chemistry. The simulation was done in two ways. First, we assume that the peak consists of three components whose positions are fixed at the literature values for the bond lengths and where the widths of the three components do not change with doping. Second, we repeated the simulation by changing the positions and widths of the subpeaks using values obtained from the XAFS results. In both ways, the intensity of each subpeak is governed by the expected concentration from the CON model, which is scaled by the appropriate product of the scattering amplitudes of the components. A simulated PDF peak was produced from these models by summing together the three subcomponents. Similar to the experimental data, the resulting simulated peak for each composition was then fitted using one Gaussian convoluted with a Sinc function. Figure 7 shows a representative plot of the fits to the experimental and simulated first PDF peak.

The average positions of the first PDF peak, for both experimental and simulated data, for all the samples, are shown in Fig. 8. The red circles give the expected behavior obtained from the simulated data. This shows the behavior with no change in intrinsic peak width due to strain, but only changes due to the composition of the peak based on the chemically ordered model and assuming that $r_{Ge\text{-}Se}$ and $r_{Se\text{-}Se}$ retain their nominal values.

Figure 8 shows that the average experimental position of the first PDF peak (black symbols) agrees well with the expected one from the CON model (red symbols), with a positive deviation that starts to appear after the stoichiometric composition. No special features are seen in the position of the first PDF peak that may correlate with the IP.

Of greater interest is to look for evidence of inhomogeneous strain from a peak broadening. The experimental as well as the simulated width of the first PDF peak are plotted versus composition in Fig. 9. There is no apparent change in width, or even in the slope of the width vs doping, associated with the IP. Any change in the bond-stretching strain of the sample on passing through the IP must be below the sensitivity of the measurement. This may not be surprising as the covalent bonds are rather stiff and the sensitivity of the measurement is limited because of the multicomponent nature of the first PDF peak. The experimental width of the first PDF peak is consistent with the simulated one (based on the CON model, where the change is just due to the change in composition of the sample) and shows no correlations with the IP.

The EXAFS data also contain information about the atomic pair distributions of the near-neighbor peaks. This information can be extracted by modeling the data. Here, the relative advantage of EXAFS is that it allows the positions and widths of the individual subcomponents of the first PDF peak to be separated. The disadvantage is that parameter correlations arise because of the number of variable parameters in the fits, which can result in biased results. This was mitigated here because we had data from both Se and Ge edges. In the composition range below the stoichiometric composition, $GeSe_2$, the number of Ge-Ge homopolar bonds is no

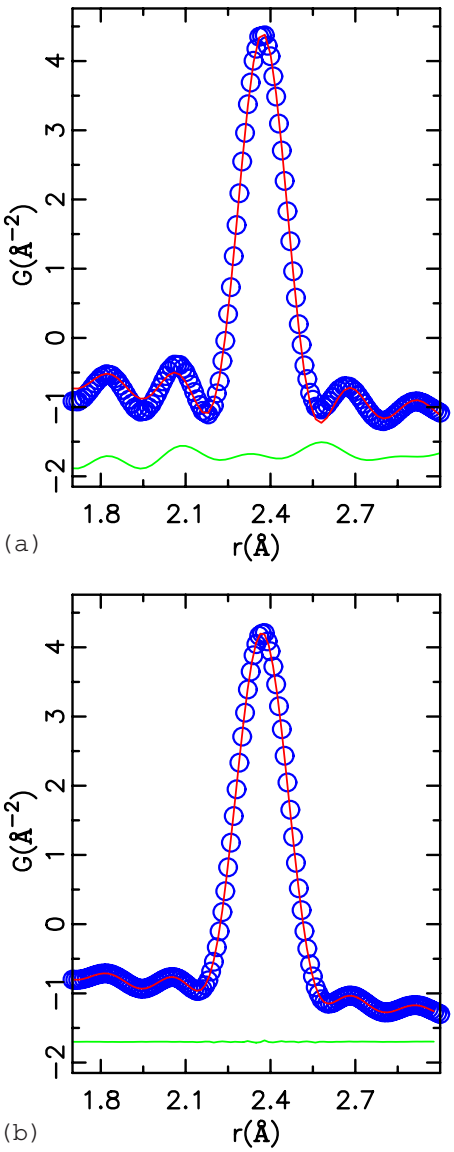

FIG. 7. (Color online) Representative plot showing the quality of the fit to the first PDF peak of the Gaussian peak (convoluted with a sinc function) in the $GeSe_2$ glass. (a) The fit to the experimental data and (b) the fit to the simulated data (see text for details). Experimental or simulated data, blue circles; the fit, red curves through the data. Offset below are the differences (green curves offset below).

more than a few percent.[34] We concentrated our analysis of the EXAFS data to this region, neglecting the contribution coming from any Ge-Ge component. The nearest neighbor coordination shell of the Ge-edge data, therefore, consists of only Ge-Se bonds, whereas that of the Se edge contains Ge-Se and Se-Se bonds. These edges were fitted together, as described below, which allowed us to extract parameters from these edges with greater reliability.

In the analysis of the XAFS data, a single scattering path was used for each bond type. At the Ge edge, and according to the CON model, only Ge-Se bonds exist, for $x \leqslant 0.33$, and so, a single scattering path of Ge tetrahedrally coordinated with Se atoms was used. For the Se-edge data, two single scattering paths were used to account for Se-Se and Se-Ge

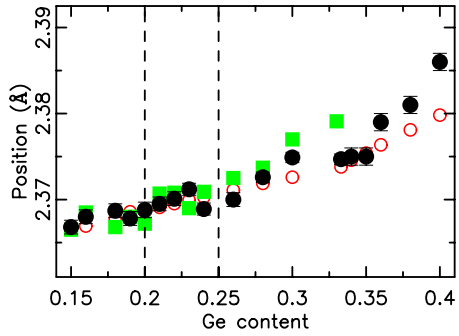

FIG. 8. (Color online) Position of the first PDF peak as obtained from fitting the experimental PDF data with a single Gaussian (black filled circles) and from fitting a simulated PDF peak based on the XAFS results (green filled squares) and CON model (red open circles). See text for details.

bonds. Ge-Se and Se-Ge path parameters were set to satisfy the bond consistency relation and the "$8-N$" rule and to share the path length and Debye–Waller factors.

Figure 10 shows the refined bond lengths and Debye–Waller factors (σ) for both Ge-Se and Se-Se bonds as a function of Ge content. The bond lengths of the subpeaks are close to their nominal values and almost constant with Ge content. On the other hand, the Debye–Waller factors for the Ge-Se bond are also constant with Ge content, but the Se-Se Debye–Waller factors decrease with Ge content. This may be an artifact that is amplified by the decreasing number of Se-Se correlations with increasing doping. No clear correlation exists with the IP, as we expect a minimum to occur in σ for the IP compositions (0.20–0.25 in Ge content) or at least an increase in σ in the stressed rigid phase at high x.

We would like to compare the results of the EXAFS with those from the PDF to check for consistency. They cannot be directly compared because the subcomponents are not resolved in the PDF data. However, the EXAFS data contain both bond length and peak width for the individual subcomponents. Therefore, it is possible to simulate the first peak in the diffraction PDFs directly from the EXAFS data by summing together the properly weighted subcomponent peaks.

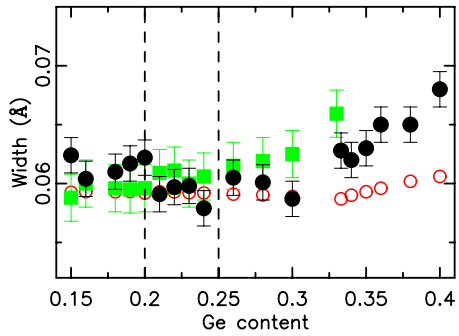

FIG. 9. (Color online) Width of the first PDF peak as obtained from fitting the experimental PDF data with a single Gaussian (black filled circles) and from fitting a simulated PDF peak based on the XAFS results (green filled squares) and CON model (red open circles). See text for details.

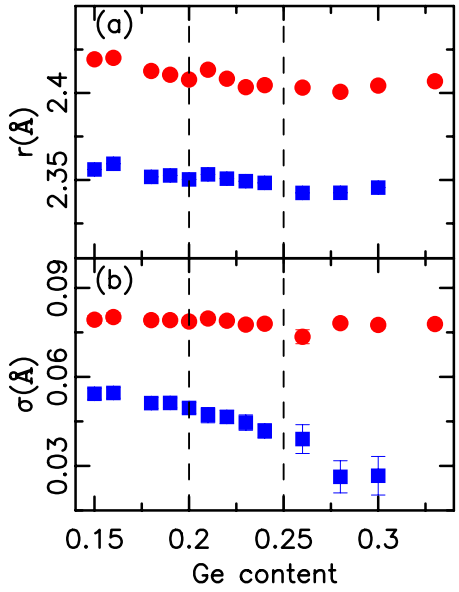

FIG. 10. (Color online) (a) Refined bond lengths and (b) Debye–Waller factors versus x (Ge content). Red circles represent Ge-Se bonds and blue squares represent Se-Se bonds. The vertical dashed lines are plotted at the lower and upper boundaries of the IP.

This was done and the resulting curves were fitted using the same protocol that was used to fit the PDF data and the simulated peak from the CON model. The results are shown by the green symbols in Fig. 8. There is good quantitative agreement with both the diffraction PDF and the result simulated from the CON model. It is interesting to note that the

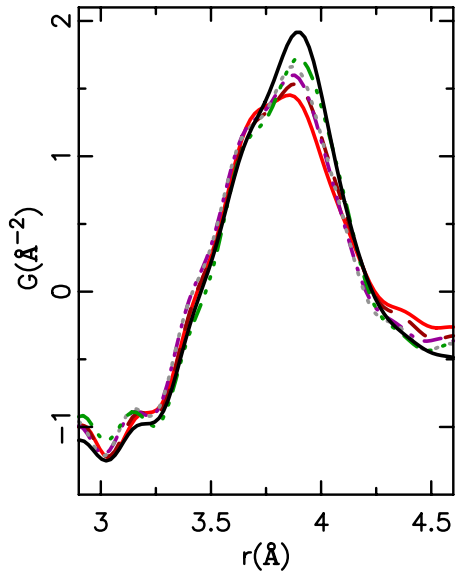

FIG. 11. (Color online) Second PDF peak plotted on an expanded scale for a selection of the samples [x=0.15, red (gray) solid line; x=0.20, dark red dashed line; x=0.23, magenta dot-dashed line; x=0.26, gray dotted line; x=0.33, dark green dot-dot-dot-dashed line; and x=0.40, black solid line]. The peak contains multiple contributions and so changes shape and position with changing composition.

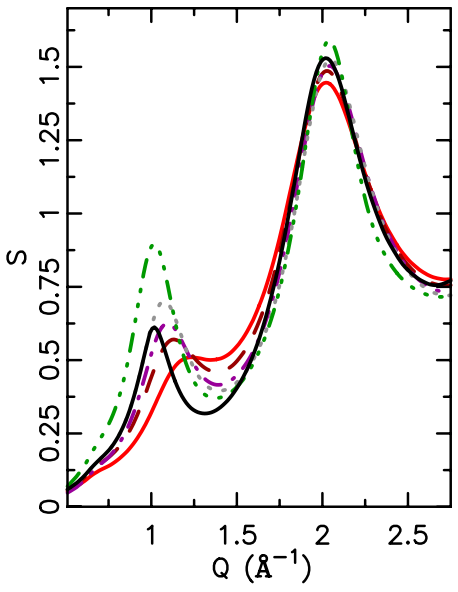

FIG. 12. (Color online) Low-Q part of the structure function [$S(Q)$] for selected samples [x=0.15, red (gray) solid line; x=0.20, dark red dashed line; x=0.23, magenta dot-dashed line; x=0.26, gray dotted line; x=0.33, dark green dot-dot-dot-dash line; and x=0.40, black line]. With increasing Ge content, the first sharp diffraction peak develops in height and shifts to the left until it reaches the stoichiometric composition (x=0.33). At higher Ge content, it decreases in height.

EXAFS results indicate that both Se-Se and Ge-Se bonds get slightly shorter with increasing Ge content, but the position of the compound peak shifts to higher r with doping. This is a result of the fact that the contribution of the longer Ge-Se bond increases with x.

Bond-bending forces in covalent materials are much weaker than bond-stretching forces[32] and so we would expect to see a larger response of second and higher neighbor peaks in the PDF due to a change in the stress state of the sample at the IP. Unfortunately, the second neighbor peak has multiple contributions and the interpretation of changes in peak width, shape, and position are somewhat ambiguous. This peak does exhibit significant changes with composition, which can be seen in Fig. 11. These are thought to be related to an evolution of the underlying network connectivity, such as the appearance of edge-sharing $GeSe_4$ tetrahedra[35] as well as effects due to benign compositional changes. This peak is mainly composed of Se-Se correlations within each tetrahedron and a left side shoulder that is due to Ge-Ge correlations among corner and edge shared tetrahedra.

Another important structural indicator that is sensitive to intermediate range order in a glass is the FSDP.[36,37] A response of this peak to the IP may indicate an underlying structural ordering, which is consistent with the idea that the finite width of the IP is a response of the system to remove strain by introducing structural ordering.

Figure 12 shows the $S(Q)$'s for some selected samples in the FSDP region. A dramatic change in the height and position of the FSDP is clearly observed, which is in agreement with earlier studies.[37] As evident in Fig. 12, the FSDP is a

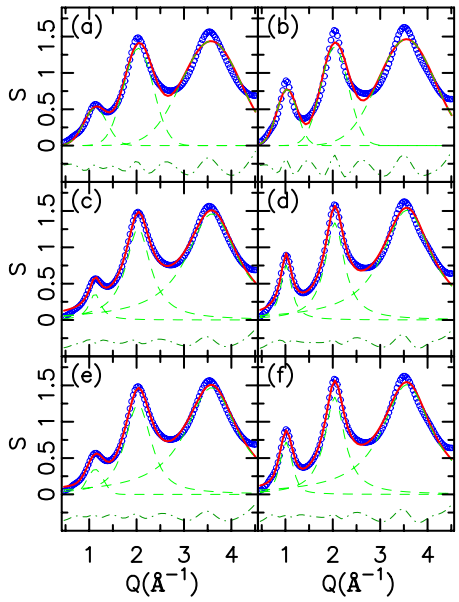

FIG. 13. (Color online) Plots indicating the quality of the fits to $S(Q)$ data for two representative samples ($Ge_{20}Se_{80}$ in the left panels and $GeSe_2$ in the right panels) using three different fitting protocols: [(a) and (b)] Pure Gaussians, [(c) and (d)] pure Lorentzians, and [(e) and (f)] pseudo-Voigt type functions. Experimental data are shown as circles, red solid curves represent the fits with the (dashed green) curves being the constituent curves of the fit, and the gray dot-dashed difference curves offset below.

strongly varying function of composition, rising out of a smoothly varying background when Ge is added to selenium glass.

Model independent peak fitting was performed on the $S(Q)$ spectra to extract the FSDP parameters (position, area, width, and height). Due to the uncertainty of the FSDP profile shape and background, the $S(Q)$ spectra were analyzed by using different fitting protocols. By doing this we can build confidence about which results are dependent on the fitting protocol, and which are robust to details of the fitting and more likely, therefore, to be physical.

All the fitting protocols included the first three peaks in the $S(Q)$ curves, with the fitting range extending from 0.5 to 4.5 Å^{-1}, and used a zero background. The three different fitting protocols that we report involved using different peak-shape functions and fixing different parameters in the fits: (a) all peaks purely Gaussian, (b) all peaks purely Lorentzian, (c) pseudo-Voigt peak shape, and (d) as (c) but the FSDP is constrained to be purely Gaussian. Other protocols were also tried, but did not change the conclusions reported here. We only consider the physical implications and report the results from the first sharp diffraction peak, and so the fits to the second and third peaks only serve to give a more accurate estimation of the FSDP parameters. Any nonzero background at higher values of Q is therefore assumed to be accounted for by the fits to higher-Q peaks. The qualities of the respective fitting protocols can be assessed from Fig. 13, which shows representative fits for two representative sample compositions and the three fitting protocols described above. The fits of pure Gaussians to all three peaks

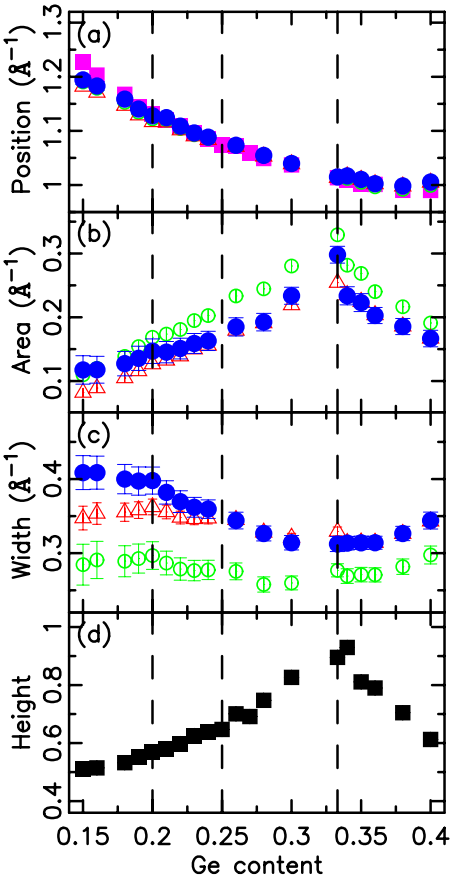

FIG. 14. (Color online) Fit parameters for the FSDP in binary Ge_xSe_{1-x} glasses as a function of x: (a) position, (b) area, (c) width, and (d) height. The different colors represent the different fitting protocols: green open circles, pure Lorentzian fits; red open triangles, pseudo-Voigt but with the FSDP constrained to be Gaussian; and blue solid circles, pseudo-Voigt with the FSDP line shape being allowed to change between Gaussian and Lorentzian as part of the fit. Square symbols in (a) and (d) represent the position and height of the FSDP, respectively, which are obtained directly from the experimental data. The dashed vertical lines are plotted at the proposed boundary of the IP as well as at the stoichiometric composition ($GeSe_2$).

were qualitatively worse than the others and so we do not consider them further.

Figure 14 shows the results of the FSDP parameters as obtained from the different fitting protocols. The results from more than one fitting protocol are included to assess the variability of the results. We have greater confidence in the results that are reproduced between the different fitting protocols. We did not include the results of the pure Gaussian fits as these fits did not reproduce the FSDP profile shape.

In each plot in Fig. 14, the green symbols are the results for Lorentzian line shapes and the red and blue are the results of pseudo-Voigt fits. In the case of the red symbols, the first peak was constrained to be purely Gaussian, but the mixing coefficients in the pseudo-Voigt function were allowed to float for the other peaks, allowing the peak to have a line shape intermediate between Gaussian and Lorentzian. In the case of the blue symbols, the pseudo-Voigt mixing param-

eters were allowed to vary for all three peaks that were fitted. The square symbols in Figs. 14(a) and 14(d) are independent fitting parameters for the (a) position and (d) peak height, which were obtained directly from the data as the x and y coordinates of the maximum of the FSDP feature. They track the fits rather well.

Qualitatively, the general behavior of each of the FSDP parameters is well reproduced by the different fitting protocols. The positions obtained by the different protocols are within the estimated uncertainties. This is not so for the width and integrated areas. The differences are largest in the low Ge-content region, where the FSDP is quite indistinct. In this region, the different fitting protocols give results with slightly different slopes. In the case of the purely Lorentzian line shapes, the widths and areas are offset over the whole range, though detailed x dependencies on the refined parameters are reproduced. Below, we discuss each parameter in detail.

The position of the FSDP tells about characteristic periodicities in the structure in real space. Figure 14(a) shows the behavior of the position of the FSDP in Ge_xSe_{1-x} glasses as a function of x. It starts at about 1.2 $Å^{-1}$ for a low Ge content, and then shifts toward lower-Q values as Ge content is increased, reaching 1.0 Å at $x=0.4$. This position corresponds to a real space length, $d=2\pi/Q_{FSDP}=5.2-6.3$ Å, which corresponds well to that of the interlayer Bragg peaks seen in crystalline $GeSe_2$,[38] where d is called the interlayer separation or cluster radius.[38,39] This is in agreement with a more elaborate wavelet analysis of the FSDP by Uchino *et al.*[40]

No anomalies in the FSDP position were detected for samples in the vicinity of the IP or at its upper boundary ($x=0.25$).

The area of the FSDP shows a maximum at the stoichiometric composition ($x=0.33$) as shown in Fig. 14(b). This is also apparent in the height of the FSDP maximum directly obtained from the data without fitting. These two parameters track each other because the width of the FSDP is nearly constant [Fig. 14(c)]. The increasing integrated area associated with the FSDP suggests that the proportion of the sample contributing to this periodicity in the structure increases with Ge content up to the stoichiometric composition, and then decreases.

Molecular dynamics[41,42] calculations indicate the importance of Ge-Ge correlations to this feature in the scattering. Therefore, it is not surprising that the peak intensity scales with the concentration of Ge in the sample being studied.

The dramatic change of the FSDP height as well as area at $x=0.33$, even though the Ge content still increases, is attributed to the change in the role of Ge atoms in the network. Below $x=0.33$, Ge atoms work as network formers,[37] so adding Ge will result in a progressive increase in the correlations contributing to this peak, which are thought to come from well-defined separations of $GeSe_4$ tetrahedra. On the contrary, above $x=0.33$, Ge atoms work as network modifiers.[37] This will weaken the ordering of the $GeSe_4$ tetrahedra and, hence, decrease the intensity of this peak. This effect is also seen when silver ions are added to g-$GeSe_2$,[43] where they modify the $GeSe_2$ covalent network by bonding to the Se atoms, with the effect of breaking up the larger ring structure and, hence, reducing the intensity of the FSDP.

The IP is thought to be rigid but unstrained, where the stress-free state was proposed to be due to self-organization in the network. If this is correct, then we might expect that the range of the IRO is maximal in the IP window. This would be characterized by a minimum in the FSDP peak width. Actually, the FSDP width is quite composition independent from the fits. There is a broad weak minimum that has a global minimum at the $GeSe_2$ composition. This suggests that the correlation length of the intermediate range order coming from the stacking of $GeSe_4$ tetrahedra is greatest for the stoichiometric composition and then decreases at higher compositions. There is a suggestion of a change in the slope of FSDP width vs x, which is associated with the rigid-floppy transition at $x=0.2$. This is certainly a suggestion that the range of the IRO starts to increase only after the rigidity of the network percolates. Apart from offsets due to parameter correlations, this kink in the curve is reproduced in all the fitting protocols, which builds confidence in its correctness. However, the FSDP width continues to decrease (the range of the IRO continues to increase) with increasing Ge content above the upper limit of the IP, so there is no convincing evidence that this is a signature for the IP.

The study of the FSDP as an observable for the IP has been pursued in two earlier studies.[17,44] The study by Sharma *et al.*[17] of the FSDP in Ge_xSe_{1-x} suggested that there were three well resolved structural phases consistent with the IP. They found a plateaulike behavior of the inverse of the FSDP position in the region of the IP. This is not reproduced in the current work. Wang *et al.*[44] concluded that around the stiffness threshold, the area of the FSDP has a plateaulike gradual decrease with x followed by a rapid decrease at $x \leqslant 0.18$. There is also no evidence of this behavior in the present study. We are not sure of the reason for this discrepancy. However, we took great care in establishing the quality of our samples and characterizing the behavior through the nonreversing heat-flow measurements. We also report multiple fitting protocols to establish the reproducibility and uncertainty of the results. This is also the only study that combines PDF and EXAFS data to address this issue. The EXAFS and PDF data are in good agreement, which gives us confidence that the current results are reliable.

IV. INTERMEDIATE RANGE ORDER

Salmon *et al.*[45] observed intermediate range order in glassy GeO_2 and $ZnCl_2$ systems. They extracted the logarithm of the partial PDFs and, intriguingly, observed periodic variations up to 25 Å for both these glasses, with a common decay length and periodicity comparable to the diameter of the larger (electronegative) species.[45] This motivated us to look at the behavior of the logarithm of $|G(r)|$ in order to find evidence of intermediate range order in the GeSe system. In Fig. 15, we show the logarithm of $|G(r)|$ for $GeSe_2$. It displays the expected behavior of trending downward with increasing r. A subtle periodicity is observed up to at least 16 Å, where the data start to get noisy, similar to that observed by Salmon *et al.*[45] The oscillations are less clear, possibly because we are examining the full $G(r)$ rather than an extracted partial PDF.

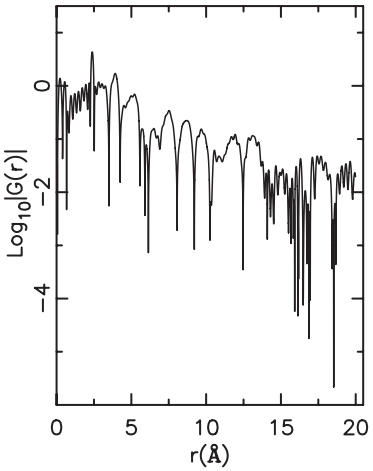

FIG. 15. $\mathrm{Log}_{10}(|G(r)|)$ versus r for $GeSe_2$.

In Fig. 16, we show logarithms of $|G(r)|$ for each composition in our dataset. At short range ($\leqslant$10 Å), there are no clear differences between the different compositions and, hence, no signature of IP. From about 14 Å up at long range, the data become very noisy. In the distance range at around 10–11 Å, there is a clear change in $\log(|G(r)|)$ for compositions from $Ge_{19}Se_{81}$ up to about $Ge_{28}Se_{72}$, which takes the form of an increased number of cusps. This could be taken as a signature of a modification in intermediate range order roughly in the vicinity of the IP. However, the result should be treated with some caution. Cusps in the $\log(|G(r)|)$ function occur when $G(r)$ crosses zero. A relatively flat region of the $G(r)$ function, close in value to zero but modulated by noise ripples, will result in a high density of cusps. This is the behavior in the high-r region above 14 Å or so. The appearance of a similar noise in the 10–11 Å region indicates a flattening of the $G(r)$ function close enough to zero for the noise to cross or, alternatively, an increase in the amplitude of the noise in this region. It is notable that this happens for a series of samples in the vicinity of the IP, but we hesitate to attribute meaning to it as there are a number of extrinsic effects that could also result in this behavior.

A structural signature of the IP that involves variations in the intermediate range, rather than the near-neighbor region, is consistent with theoretical work of Sartbaeva *et al.*,[12] which shows that rigidity properties in the GeSe system are influenced by variations in the lengths of the Se chains connecting nodal (Ge) atoms. A more detailed study including the extraction of Bhatia–Thornton partial PDFs for the GeSe system would be required before any conclusions can be drawn on the medium range order in the IP.

V. SUMMARY AND CONCLUSIONS

A careful composition dependent study of the structure of Ge_xSe_{1-x} glasses, through the composition range associated with the intermediate phase and using high energy x-ray total scattering studies coupled with EXAFS measurements at the Ge and Se edges, does not yield evidence of a structural origin for the IP. Structural parameters associated with strain in the sample (pair distribution function peak widths from the x-ray and EXAFS data) and intermediate range order [the first sharp diffraction peak in $S(Q)$] all evolve smoothly with composition, and no discontinuities or breaks in slope are evidently associated with the boundaries of the IP.

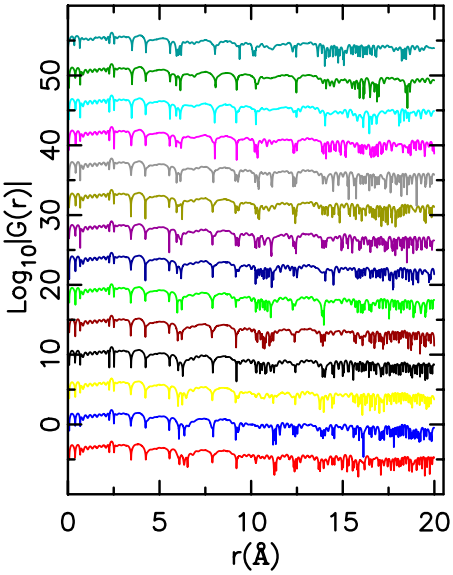

FIG. 16. (Color online) $\mathrm{Log}_{10}(|G(r)|)$ versus r for different compositions, offset along the y axis. The compositions (x) are, from the bottom to the top curves, 0.15, 0.16, 0.18, 0.19, 0.20, 0.21, 0.22, 0.23, 0.24, 0.26, 0.28, 0.30, 0.33, and 0.34.

ACKNOWLEDGMENTS

We would like to acknowledge discussions with G. T. Barkema and S. A. Wells, and help from Douglas S. Robinson at the 6-ID beamline of the Advanced Photon Source (APS) and Qing Ma at the 5-BM beamline of the APS for help in setting up the experiments. We also thank Billinge group members for help in collecting the data. Work at Michigan State was supported by U.S. Department of Energy through Grant No. DE-FG02-97ER45651. Work at Arizona State was supported by NSF through Grants No. DMR 0703940 and DMR 0703973. Work at U. Cincinnati was supported by NSF through Grant No. DMR 0456472. PDF data were collected at the 6ID-D beamline in the Midwest Universities Collaborative Access Team (MUCAT) sector at the APS. Use of the APS is supported by the U.S. DOE, Office of Science, Office of Basic Energy Sciences, under Contract No. W-31-109-Eng-38. The MUCAT sector at the APS is supported by the U.S. DOE, Office of Science, Office of Basic Energy Sciences, through the Ames Laboratory under Contract No. W-7405-Eng-82. EXAFS experiments were performed at the DND-CAT at Sector 5 of the APS at Argonne National Laboratory. DND-CAT is supported by the E. I. DuPont de Nemours & Co., the Dow Chemical Company, the U.S. National Science Foundation through Grant No. DMR-9304725, and the State of Illinois through the Department of Commerce and the Board of Higher Education Grant No. IBHE HECA NWU 96.

*Present address: Department of Physics, University of Jordan, Amman 11942, Jordan.
†Present address: Department of Applied Physics and Applied Mathematics, Columbia University, New York, New York 10027; sb2896@columbia.edu

[1] J. C. Phillips, J. Non-Cryst. Solids **34**, 153 (1979).
[2] J. C. Phillips, J. Non-Cryst. Solids **43**, 37 (1981).
[3] M. F. Thorpe, J. Non-Cryst. Solids **57**, 355 (1983).
[4] W. A. Kamitakahara, R. L. Cappelletti, P. Boolchand, B. Halfpap, F. Gompf, D. A. Neumann, and H. Mutka, Phys. Rev. B **44**, 94 (1991).
[5] M. Tatsumisago, B. L. Halfpap, J. L. Green, S. M. Lindsay, and C. A. Angell, Phys. Rev. Lett. **64**, 1549 (1990).
[6] U. Senapati and A. K. Varshneya, J. Non-Cryst. Solids **185**, 289 (1995).
[7] X. W. Feng, W. J. Bresser, and P. Boolchand, Phys. Rev. Lett. **78**, 4422 (1997).
[8] D. Selvanathan, W. J. Bresser, and P. Boolchand, Phys. Rev. B **61**, 15061 (2000).
[9] M. V. Chubynsky, M.-A. Briere, and N. Mousseau, Phys. Rev. E **74**, 016116 (2006).
[10] M. Micoulaut, Phys. Rev. B **74**, 184208 (2006).
[11] M. F. Thorpe, D. J. Jacobs, M. V. Chubynsky, and J. C. Phillips, J. Non-Cryst. Solids **266**, 859 (2000).
[12] A. Sartbaeva, S. A. Wells, A. Huerta, and M. F. Thorpe, Phys. Rev. B **75**, 224204 (2007).
[13] L. Ross and M. Bourgon, Can. J. Chem. **47**, 2555 (1969).
[14] P. Quenez, R. Ceolin, and P. Khodadad, Bull. Soc. Chim. Fr. **1**, 117 (1972).
[15] P. Tronc, A. Brenac, and C. Sebenne, Phys. Rev. B **8**, 5947 (1973).
[16] M. M. Hafiz, F. H. Hammad, and N. A. Elkabany, Physica B **183**, 392 (1993).
[17] D. Sharma, S. Sampath, N. P. Lalla, and A. M. Awasthi, Physica B **357**, 290 (2005).
[18] P. Boolchand, X. Feng, and W. J. Bresser, J. Non-Cryst. Solids **293**, 348 (2001).
[19] L. Cai and P. Boolchand, Philos. Mag. B **82**, 1649 (2002).
[20] F. Inam, M. T. Shatnawi, D. Tafen, S. J. L. Billinge, P. Chen, and D. A. Drabold, J. Phys.: Condens. Matter **19**, 455206 (2007).
[21] P. J. Chupas, X. Qiu, J. C. Hanson, P. L. Lee, C. P. Grey, and S. J. L. Billinge, J. Appl. Crystallogr. **36**, 1342 (2003).
[22] S. D. Shastri, K. Fezzaa, A. Mashayekhhi, W.-K. Lee, P. B. Fernandez, and P. L. Lee, J. Synchrotron Radiat. **9**, 317 (2002).
[23] A. P. Hammersley, FIT2D V9.129 Reference Manual V3.1, ESRF Internal Report No. ESRF98HA01T, 1998 (unpublished).
[24] X. Qiu, J. W. Thompson, and S. J. L. Billinge, J. Appl. Crystallogr. **37**, 678 (2004).
[25] B. E. Warren, *X-ray Diffraction* (Dover, New York, 1990).
[26] T. Egami and S. J. L. Billinge, *Underneath the Bragg peaks: Structural Analysis of Complex Materials* (Pergamon, Oxford, England, 2003).
[27] M. Newville, J. Synchrotron Radiat. **8**, 322 (2001).
[28] B. Ravel and M. Newville, J. Synchrotron Radiat. **12**, 537 (2005).
[29] M. Newville, P. Livins, Y. Yacoby, J. J. Rehr, and E. A. Stern, Phys. Rev. B **47**, 14126 (1993).
[30] D. E. Sayers and E. A. Stern, Phys. Rev. Lett. **27**, 1204 (1971).
[31] V. Petkov, I. K. Jeong, J. S. Chung, M. F. Thorpe, S. Kycia, and S. J. L. Billinge, Phys. Rev. Lett. **83**, 4089 (1999).
[32] I.-K. Jeong, F. Mohiuddin-Jacobs, V. Petkov, S. J. L. Billinge, and S. Kycia, Phys. Rev. B **63**, 205202 (2001).
[33] G. Lucovsky, F. L. Galeener, R. H. Geils, and R. C. Keezer, *The Structure of Non-crystalline Materials*, 1st ed. (Taylor & Francis, London, 1977).
[34] I. Petri, P. S. Salmon, and H. E. Fischer, Phys. Rev. Lett. **84**, 2413 (2000).
[35] I. T. Penfold and P. S. Salmon, Phys. Rev. Lett. **67**, 97 (1991).
[36] S. R. Elliott, Phys. Rev. Lett. **67**, 711 (1991).
[37] E. Bychkov, C. J. Benmore, and D. L. Price, Phys. Rev. B **72**, 172107 (2005).
[38] M. Jergel and P. Mrafko, Phys. Status Solidi A **83**, 113 (1984).
[39] S. R. Elliott, *Physics of Amorphous Materials*, 1st ed. (Longmans, London, 1984).
[40] T. Uchino, J. D. Harrop, S. N. Taraskin, and S. R. Elliott, Phys. Rev. B **71**, 014202 (2005).
[41] P. Vashishta, R. K. Kalia, and I. Ebbsjo, Phys. Rev. B **39**, 6034 (1989).
[42] P. Vashishta, R. K. Kalia, G. A. Antonio, and I. Ebbsjo, Phys. Rev. Lett. **62**, 1651 (1989).
[43] D. L. Price, S. Susman, K. J. Volin, and R. J. Dejus, Physica B **156**, 189 (1989).
[44] Y. Wang, E. Ohata, S. Hosokawa, M. Sakurai, and E. Matsubara, J. Non-Cryst. Solids **337**, 54 (2004).
[45] P. S. Salmon, A. C. Barnes, R. A. Martin, and G. J. Cuello, Phys. Rev. Lett. **96**, 235502 (2006).